



Hybrid electro-optic modulator combining silicon photonic slot waveguides with high-k radio-frequency slotlines

SANDEEP UMMETHALA,^{1,2,7}  JUNED N. KEMAL,¹  AHMED S. ALAM,¹  MATTHIAS LAUERMANN,¹ ARTEM KUZMIN,³ YASAR KUTUVANTAVIDA,¹ SREE H. NANDAM,⁴ LOTHAR HAHN,² DELWIN L. ELDER,⁵ LARRY R. DALTON,⁵ THOMAS ZWICK,⁶ SEBASTIAN RANDEL,¹ WOLFGANG FREUDE,¹  AND CHRISTIAN KOOS^{1,2,*} 

¹Karlsruhe Institute of Technology (KIT), Institute of Photonics and Quantum Electronics (IPQ), 76131 Karlsruhe, Germany

²Karlsruhe Institute of Technology (KIT), Institute of Microstructure Technology (IMT), 76334 Eggenstein-Leopoldshafen, Germany

³Karlsruhe Institute of Technology (KIT), Laboratory for Applications of Synchrotron Radiation (LAS), 76131 Karlsruhe, Germany

⁴Karlsruhe Institute of Technology (KIT), Institute of Nanotechnology (INT), 76334 Eggenstein-Leopoldshafen, Germany

⁵University of Washington, Department of Chemistry, Seattle, Washington 98195, USA

⁶Karlsruhe Institute of Technology (KIT), Institute of Radio Frequency Engineering and Electronics (IHE), 76131 Karlsruhe, Germany

⁷e-mail: sandeep.ummethala@kit.edu

*Corresponding author: christian.koos@kit.edu

Received 5 October 2020; revised 21 January 2021; accepted 25 January 2021 (Doc. ID 411161); published 9 April 2021

Electro-optic (EO) modulators rely on the interaction of optical and electrical signals with second-order nonlinear media. For the optical signal, this interaction can be strongly enhanced using dielectric slot-waveguide structures that exploit a field discontinuity at the interface between a high-index waveguide core and the low-index EO cladding. In contrast to this, the electrical signal is usually applied through conductive regions in the direct vicinity of the optical waveguide. To avoid excessive optical loss, the conductivity of these regions is maintained at a moderate level, thus leading to inherent RC limitations of the modulation bandwidth. In this paper, we show that these limitations can be overcome by extending the slot-waveguide concept to the modulating radio-frequency (RF) signal. Our device combines an RF slotline that relies on BaTiO₃ as a high-k dielectric material with a conventional silicon photonic slot waveguide and a highly efficient organic EO cladding material. In a proof-of-concept experiment, we demonstrate a 1 mm long Mach-Zehnder modulator that offers a 3 dB bandwidth of 76 GHz and a 6 dB bandwidth of 110 GHz along with a small π voltage of 1.3 V ($U_{\pi} L = 1.3$ V mm). We further demonstrate the viability of the device in a data-transmission experiment using four-state pulse-amplitude modulation (PAM4) at line rates up to 200 Gbit/s. Our first-generation devices leave vast room for further improvement and may open an attractive route towards highly efficient silicon photonic modulators that combine sub-1 mm device lengths with sub-1 V drive voltages and modulation bandwidths of more than 100 GHz. © 2021 Optical Society of America under the terms of the OSA Open Access Publishing Agreement

<https://doi.org/10.1364/OPTICA.411161>

1. INTRODUCTION

High-speed electro-optic (EO) modulators are key devices for optical communications [1–3], optical metrology [4], microwave photonics [5], or ultra-broadband signal processing at THz bandwidths [6]. Ideal modulators should combine small π -voltages U_{π} , low insertion losses α , and short device lengths L with large modulation bandwidths, while offering a path to cost-efficient mass production and monolithic co-integration with advanced photonic circuitry. In practice, however, it is challenging to fulfill all these requirements simultaneously. When it comes to scalability and high-density integration, the silicon photonic (SiP) platform would be the technology of choice, exploiting highly mature CMOS processes and offering a rich portfolio of advanced

photonic devices that can be realized with high yield on large-area wafers [7]. However, due to the absence of the Pockels effect in silicon, conventional SiP modulators rely on carrier injection or depletion in $p-n$ junctions that are integrated into the optical waveguides [8]. This leads to an inherent trade-off between device efficiency and modulation bandwidth. As an example, depletion-type SiP modulators were demonstrated with bandwidths up to 48 GHz, but the efficiency of these devices was rather low with $U_{\pi} L$ products of 7.4 V mm [9]. The efficiency of SiP modulators can be greatly improved by combining low-loss slot waveguides on silicon-on-insulator (SOI) with optimized organic electro-optic materials in a hybrid approach [10,11]. These so-called silicon-organic hybrid (SOH) devices can benefit from ultra-high in-device electro-optic coefficients of, e.g., 390 pm/V, leading to

ultra-low voltage-length products down to $U_\pi L = 0.32$ V mm [12]. However, without a supporting gate voltage [13], the EO bandwidth of experimentally demonstrated slot-waveguide SOH modulators is limited [14] to, e.g., 25 GHz or less [15] due to the RC time constant associated with the capacitance of the slot and the resistance of the adjacent doped silicon (Si) slabs adjacent to the slot waveguide [14]. Plasmonic-organic hybrid (POH) Mach–Zehnder modulators (MZMs) [6,11,16–18] can overcome these limitations by replacing the doped silicon slabs with highly conductive gold pads and by exploiting surface plasmon polaritons in the resulting metallic slot waveguide. This, however, comes at the price of substantial optical losses α , leading to rather high loss-efficiency products [11] $\alpha U_\pi L$ of more than 10 V dB [6,19] as compared to 1 V dB for SOH devices [12,20]. Other integration platforms such as thin-film lithium-niobate have shown impressive modulation bandwidths of up to 100 GHz [21], but their efficiency is limited by rather high voltage-length products $U_\pi L$ in excess of 20 V mm [21], and monolithic co-integration with other devices is difficult. Modulators based on indium phosphide (InP) can also offer large bandwidths of, e.g., 80 GHz [22], but the voltage-length products of more than 6 V mm are still comparatively high, and fabrication relies on rather expensive processes that cannot compete with the scalability and maturity of the silicon photonic platform. Thus, a scalable approach to realize highly efficient and low-loss modulators with large electro-optic bandwidth is still lacking.

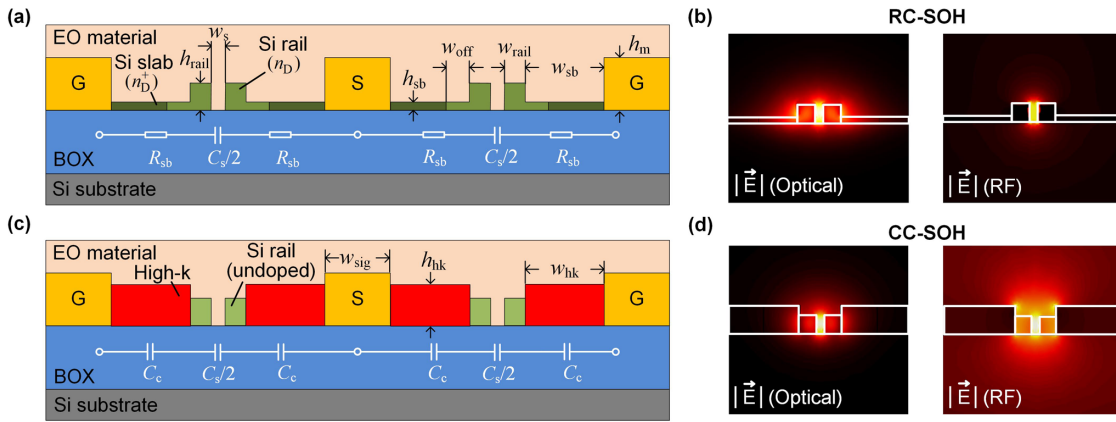
In this paper, we report on a novel concept for hybrid silicon photonic modulators that allows combining the high efficiency of organic electro-optic materials with large modulation bandwidths without the need for lossy plasmonic structures. The device overcomes the RC limitations of conventional SOH slot-waveguide modulators by replacing resistive coupling through the doped Si slabs with capacitive coupling via high- k dielectric material [23]. In a proof-of-concept experiment, we demonstrate a 1 mm long capacitively coupled SOH (CC-SOH) Mach–Zehnder modulator that exploits barium titanate (BaTiO_3) as high- k dielectric and simultaneously offers a large EO bandwidth of 76 GHz and a small π -voltage of 1.3 V ($U_\pi L = 1.3$ V mm). To validate the viability of the device, we generate a four-state pulse-amplitude modulation (PAM4) signals at symbol rates (line rates) up to 100 GBd (200 Gbit/s) with bit-error ratios (BERs) below the threshold for soft-decision forward error correction. As our first-generation devices are not yet optimized and leave vast room for further improvement, we believe that the CC-SOH concept opens an attractive route towards highly efficient silicon photonic modulators that combine sub-1 mm device lengths with sub-1 V drive voltages, sub-1 dB phase-shifter losses, and modulation bandwidths of 100 GHz or more.

2. SOH MODULATOR: RESISTIVE VERSUS CAPACITIVE COUPLING

The concept of capacitively coupled silicon-organic hybrid (CC-SOH) modulators and their advantages over resistively coupled SOH (RC-SOH) devices are explained in Fig. 1. Figure 1(a) shows the cross section of a conventional RC-SOH MZM [11], realized on a silicon-on-insulator (SOI) substrate. Each arm of the MZM comprises a silicon (Si) slot waveguide formed by two Si rails (green), which typically feature rail widths $w_{\text{rail}} = 150 \dots 200$ nm and rail heights $b_{\text{rail}} = 200 \dots 400$ nm which are separated by

a slot of width $w_s = 80 \dots 200$ nm. The radio-frequency (RF) modulating signal is carried by a coplanar transmission line (yellow) in ground–signal–ground (GSG) configuration. The Si rails are connected to the metal trace of the transmission line via doped Si slabs (dark green) having typical heights $b_{\text{sb}} = 50 \dots 70$ nm and widths $w_{\text{sb}} = 1.2 \dots 2.0$ μm . The slot region is filled with an organic EO material which, at near-infrared telecommunication wavelengths, has a refractive index of ($n_{\text{EO}} \approx 1.6 \dots 1.9$), much smaller than that of Si ($n_{\text{Si}} \approx 3.5$). This leads to a pronounced field enhancement of the optical quasi-transverse-electric (quasi-TE) mode in the slot region; see Fig. 1(b) [24]. At the same time, when operated at sufficiently low modulation frequencies, the voltage applied to the transmission line entirely drops across the narrow slot region. This leads to a tight confinement of the electric RF field to the slot, see Fig. 1(b), and ensures strong overlap with the optical mode, which results in high modulation efficiency; see Section 1 of Supplement 1 for details. The concept of RC-SOH MZM opens a path towards compact devices with sub-1 mm phase-shifter lengths and sub-1 V operation voltages [12,20] that can be directly driven by highly scalable CMOS circuits without the need for a separate amplifier [25]. At high operation frequencies, however, the slot capacitance cannot be fully charged and discharged through the resistive slabs during one modulation cycle [14]. For a quantitative description of the RC-SOH MZM dynamics, we use a simple equivalent-circuit model, illustrated as a white overlay in Fig. 1(a). Each of the two slot waveguides is represented by a slot capacitance $C_s/2$, which is connected to the metal transmission line through a total slab resistance $2R_{\text{sb}}$. Taking into account the contribution of both arms, this results in an intrinsic RC -limited bandwidth $f_{\text{RC}} = 1/(2\pi R_{\text{sb}} C_s)$ for the RC-SOH MZM. High-bandwidth RC-SOH devices require low slab resistivity and hence high doping concentration, which leads to larger optical losses. This trade-off between optical loss and RC -limited bandwidth can be avoided by using a tailored doping profile, where the Si rails and the directly adjacent slab regions have lower doping concentrations n_{D} while much higher concentrations n_{D}^+ are used further away from the slot [14]; see Fig. 1(a). Still, the RC -limited bandwidth turns out to be one of the most stringent restrictions of experimentally demonstrated RC-SOH devices [15,26,27]. In laboratory experiments, this limitation could only be overcome by applying a relatively high gate voltage U_{gate} across the buried SiO_2 (BOX) layer [13] to induce a charge accumulation layer in the Si slabs. However, this gate voltage typically exceeds 100 V [13,15] and is thus not a solution for practical devices.

CC-SOH MZM overcome these limitations by avoiding the resistive slabs altogether and by using capacitive coupling instead. To this end, the doped Si slabs in Fig. 1(a) are replaced by a high- k dielectric material, which forms a large coupling capacitor between the optical slot waveguide and the metal traces of the GSG transmission line; see Fig. 1(c). The simplified equivalent circuit of this scheme is depicted as a white overlay in Fig. 1(c). Each phase modulator of the MZM is modeled by a slot capacitance $C_s/2$, which is connected to the metal transmission line through a coupling capacitance C_c to each side of the slot. If the high- k dielectric has a relative permittivity ϵ_r much larger than that of Si and the EO material such that $C_c \gg C_s$, then the RF electric field drops predominantly across the slot region. The high- k dielectric is chosen such that the refractive index for optical wavelengths is smaller than n_{Si} such that confinement of the optical mode to the slot region is not impaired, and thickness of the high- k slabs may be chosen in



the range $h_{\text{hk}} = 150 \dots 600$ nm, see Section 5 of Supplement 1, which provides a more detailed design study of CC-SOH devices and discusses also the impact of the height h_m and the signal width w_{sig} of the metal transmission-line traces. Figure 1(d) shows the electric-field profiles of the optical quasi-TE mode and RF mode of the CC-SOH phase modulator assuming a refractive index $n_{\text{hk}} = 1.85$ for the high-k dielectric; see Section 1 of Supplement 1 for details on the calculation of the optical and RF mode fields. Since the relative permittivity of the high-k dielectric ($\epsilon_{r,\text{hk}} \approx 100$) and of the Si ($\epsilon_{r,\text{Si}} \approx 11.7$) is larger than that of the EO material ($\epsilon_{r,\text{EO}} \approx 5.68$), the electric RF field in the slot region is locally enhanced. The structure thus combines a silicon photonic slot waveguide for optical frequencies with a high-k dielectric slotline for RF frequencies [28]. This leads to a strong EO interaction of the RF and the optical fields, which can be quantified by a field interaction factor Γ_s that is obtained from an overlap integral of the optical and the RF fields in the slot region; see Section 3A of Supplement 1 for details. For properly designed CC-SOH devices, these field interaction factors Γ_s can assume values that are on par with those of conventional RC-SOH devices; see Section 5 of Supplement 1 for more details on advanced CC-SOH device designs. By proper choice of high-k materials with low absorption in the near infrared [28], CC-SOH devices should hence

permit simultaneous realization of low-loss and high modulation efficiency. Examples of high-k dielectric materials with $\epsilon_r > 100$ and refractive indices n_{hk} smaller than n_{Si} are TiO_2 , SrTiO_3 , BaSrTiO_3 , and BaTiO_3 . Since the capacitive coupling between the transmission-line electrodes and the slot of an ideal CC-SOH MZM is not associated with a RC time constant, the bandwidth is only limited by the frequency-dependent propagation loss of the modulating RF signal, impedance mismatch, and the velocity mismatch between the RF and the optical wave. By an optimized traveling-wave design, CC-SOH devices thus offer a route towards low-loss, highly efficient modulators featuring large electrical bandwidths.

3. DEVICE FABRICATION AND EXPERIMENTAL DEMONSTRATION

To demonstrate the viability of the CC-SOH concept, we fabricated a 1 mm long CC-SOH MZM with amorphous BaTiO_3 (BTO) as high-k dielectric. The device is realized on an SOI substrate having a 220 nm thick Si device layer and a 2 μm thick buried oxide (SiO_2); see Section 2A of Supplement 1 for details. A schematic layout of the MZM is depicted in Fig. 2(a). Light is coupled to the SiP chip via an on-chip grating coupler (GC). A

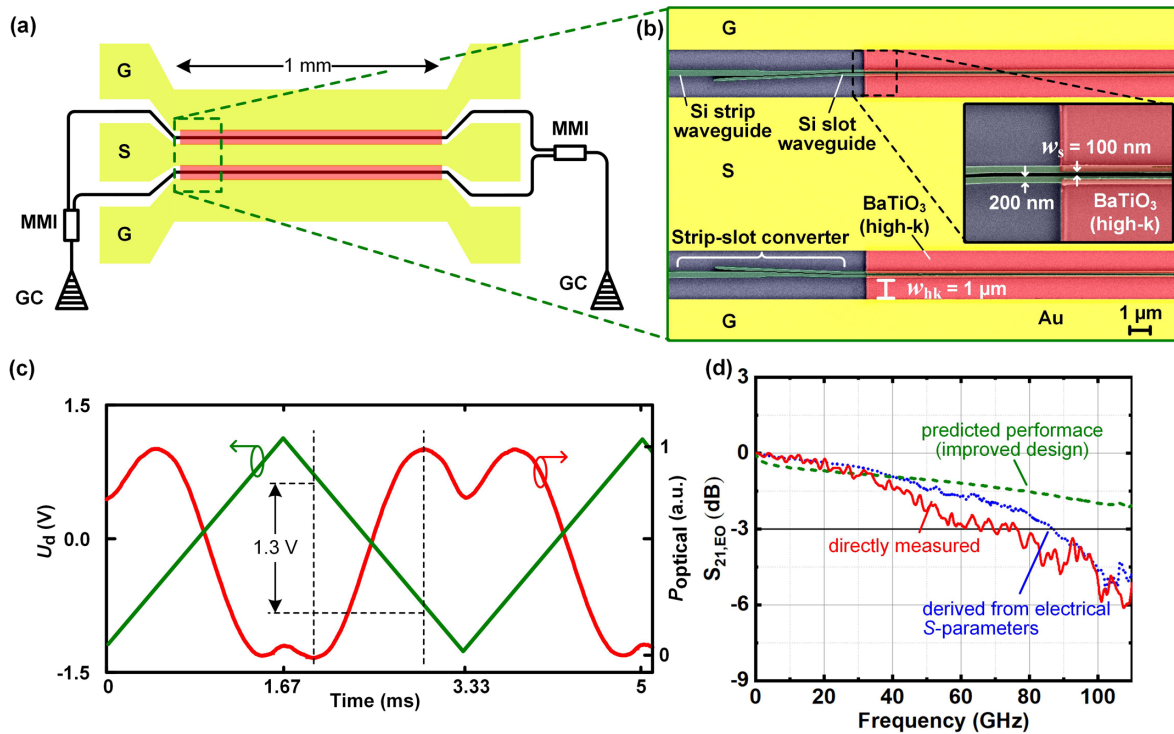


Fig. 2. Capacitively coupled SOH MZM using amorphous barium titanate (BaTiO_3 , BTO) as a high- k dielectric. (a) Schematic of a CC-SOH MZM driven by a coplanar ground-signal-ground (GSG) transmission line. Light is coupled in and out of the device via on-chip grating couplers (GC). Multimode interference (MMI) couplers are used to split and recombine the light of the two MZM arms. (b) False-colored SEM image of a CC-SOH MZM section, as defined by the dashed green rectangle in (a). Each phase-shifter arm of the MZM comprises a strip-to-slot converter (green) for coupling light from the Si strip waveguide to the Si slot waveguide. A coplanar ground-signal-ground (GSG) transmission line made from gold (yellow) carries the RF signal. Amorphous BTO slabs (red) having a height of 150 nm and a width of $w_{hk} = 1 \mu\text{m}$ are deposited between the Si slot waveguide and the gold strips of the coplanar transmission line. The phase-shifter section of each arm is 1 mm long. The inset shows a zoom-in of one of the MZM arms comprising a Si slot waveguide with a slot width $w_s = 100 \text{ nm}$ and between 200 nm wide Si rails. (c) Measurement of the π -voltage of a BTO-based CC-SOH MZM showing the intensity modulation at the device output (red) for a 0.3 kHz triangular drive signal (green). The π -voltage $U_\pi = 1.3 \text{ V}$ can be directly read from the voltage increment needed to drive the intensity modulation from minimum to maximum transmission. (d) Dynamic behavior of a 1 mm long CC-SOH MZM with YLD124 as EO cladding material: The red curve shows the electro-optic (EO) response $S_{21,EO}$ measured using a vector network analyzer (VNA) and a calibrated high-speed photodiode. The measured 3 dB EO bandwidth of the 1 mm long CC-SOH MZM is 76 GHz. As a reference, we also derive the EO response from the measured electrical S -parameters of the device using an analytical model [29]; see Section 3C of Supplement 1 for details. The analytically derived result is indicated by the blue curve and agrees well with the directly measured behavior. The strong frequency-dependent decay of the EO response is mainly caused by the strong RF propagation loss of the modulating signal along the coplanar transmission line having a thickness of only 150 nm. By using thicker gold strips, the bandwidth of the MZM can be significantly increased. This is indicated by the green curve, which corresponds to the predicted EO response of an improved device design that relies on 600 nm thick gold strips for the coplanar transmission line; see Section 5 of Supplement 1 for details. Such a device could offer 3 dB EO bandwidths well beyond 100 GHz.

multimode interference (MMI) coupler splits the incoming light and launches it into the two arms of an unbalanced MZM. The two arms have a path difference of $80 \mu\text{m}$ that allows for an adjustment of the operating point by tuning the wavelength. The modulating RF signal is coupled to the MZM through a coplanar transmission line, which is realized in ground-signal-ground (GSG) configuration. A second MMI at the other end of the MZM combines the modulated light and feeds it to an output waveguide, which is connected to another GC. Figure 2(b) shows a false-colored scanning electron microscope (SEM) image of a section of the CC-SOH MZM, as defined by the dashed (green) rectangle in the Fig. 2(a). Each MZM arm consists of a Si strip waveguide (width $w = 500 \text{ nm}$; height $h = 220 \text{ nm}$), which is transformed into a slot waveguide using a strip-to-slot converter [30]. The slot waveguide comprises two Si rails (green) with widths $w_{\text{rail}} = 200 \text{ nm}$, which are separated by a slot of width $w_s = 100 \text{ nm}$, see inset in Fig. 2(b). A coplanar transmission line made from 150 nm thick gold electrodes (yellow) in GSG configuration carries the RF signal.

Amorphous BTO slabs (red) having a height $h_{hk} = 150 \text{ nm}$ and a width $w_{hk} = 1 \mu\text{m}$ are deposited between the Si slot waveguide and the metal electrodes using room-temperature RF magnetron sputtering followed by a lift-off process; see Section 2A of Supplement 1 for details.

Note that, for high-performance devices, both the slab width w_{hk} and the height h_{hk} are generally subject to design trade-offs: Reducing the slab width w_{hk} increases the coupling capacitance C_c and thus increases the modulation efficiency, but also results in larger interaction of the optical mode with the metal traces of the RF transmission line and therefore results in larger optical losses. For the chosen slab width of $w_{hk} \geq 1 \mu\text{m}$, the contribution to the optical loss is of the order of 0.1 dB/mm or less, and hence does not play a significant role; see Fig. S8 and the associated discussion in Section 5 of Supplement 1 for details. Regarding the slab height, we chose a value of $h_{hk} = 150 \text{ nm}$ due to limitations of an existing lift-off process that relied on a thin PMMA resist layer and that was used for fabricating our devices. A thorough analysis of the

associated design trade-offs reveals that this value is too small and should be increased in future device generations: If the slab is too thin, the coupling capacitance will be small and the RF field does not have a good overlap with the optical mode, resulting in a reduced field interaction factor Γ_s . On the other hand, if the BTO slab is too thick, the transverse capacitance of the line will increase and lead to a reduced line impedance below the envisaged 50 Ω , while the field interaction factor saturates and does not increase further; see Section 5 of Supplement 1 for a detailed analysis. Given the fact that a certain operation voltage of the MZM is dictated by the required phase shift, a lower impedance will increase the power consumption of the device, which is undesired. A more detailed design study for improved CC-SOH devices shows that BTO films with a height of approximately $h_{\text{hk}} \approx 350$ nm would lead to a decent trade-off between these competing targets; see Section 5 of Supplement 1. Similarly, a height of $h_m = 150$ nm was chosen for the metal GSG traces to stay within the limitations of our lift-off-process, which led to significant RF propagation loss and turned out to be the main limitation of the measured bandwidth. Future device designs should use thicker traces with $h_m \geq 500$ nm that significantly reduce the RF propagation loss; see Section 5 of Supplement 1. Such improved CC-SOH devices with thicker BTO and metal layers can still be fabricated using lift-off processes based on multi-layer resists [31,32].

Over the course of our experiments, we also characterized the optical properties of the deposited amorphous BTO thin films having a refractive index of $n_{\text{BTO}} = 1.85$ at a wavelength of 1550 nm; see Section 2C of Supplement 1 for details. After fabrication of the device, an organic EO material (YLD124, $n_{\text{EO}} = 1.9$ [33]) is filled into the silicon slots. Note that the refractive indices of the BTO and EO material are very similar, ensuring a smooth transition of the optical mode without significant reflections. To orient the organic chromophores, the EO material is activated by a one-time poling process [11]. To this end, the chip is heated above the glass transition temperature of the organic EO material, and a DC voltage is applied across the floating ground electrodes to align the dipolar chromophores in the two slots. The orientation of the chromophores is frozen by cooling the chip to room temperature while maintaining the DC poling field. This leads to a configuration where the driving electric RF field applied to the GSG transmission line is parallel to the poling direction in one MZM arm and antiparallel in the other arm, thereby enabling operation of the CC-SOH MZM in push-pull mode [11].

To quantify the modulation efficiency, we measure the π -voltage U_π of the MZM by driving it with a 0.3 kHz triangular signal U_d as depicted in Fig. 2(c), green curve. The intensity-modulated output (red curve) of the MZM is detected by a photodiode and recorded along with the drive signal using an oscilloscope. We measure a voltage difference of $U_\pi = 1.3$ V that is needed to drive the transmission of the MZM from its minimum to its maximum by introducing a phase shift of π between the optical signals in the 1 mm long MZM arms, thus leading to a π -voltage-length product of $U_\pi L = 1.3$ V mm. To estimate the associated EO coefficient r_{33} of the organic EO material, we calculate the field interaction factor Γ_s for the fabricated CC-SOH structure; see Section 3B of Supplement 1. To this end, we first extract the relative permittivity $\epsilon_{r,\text{BTO}} = 18$ and the loss tangent $\tan \delta_{\text{BTO}} \approx 0.03$ of the amorphous BTO films from dedicated test structures; see Sections 2D and 2E of Supplement 1. Based on this, we calculate the distribution of the RF field using

a commercial numerical solver (CST Microwave Studio), and we estimate a field interaction factor of $\Gamma_s = 0.048$ between the RF and the optical fields through electromagnetic simulations. Using Eq. (S11) in Section 3A of Supplement 1, we calculate an electro-optic coefficient of $r_{33} \approx 180$ pm/V, which was obtained with a poling field of approximately 450 V/ μm in the slot region; see Section 3B of Supplement 1 for details. The achieved EO coefficient is in fair agreement with previously reported values for the same or similar materials. Specifically, an EO coefficient of $r_{33} \approx 242(\pm 37)$ pm/V was obtained for pure YLD124 when poling the material through adjacent dielectric layers in a thin-film experiment [34]. Similarly, for conventional RC-SOH MZM with 150 nm wide slots, in-device EO coefficients r_{33} of approximately 250 pm/V [12] were obtained using poling fields of approximately 400 V/ μm in combination with the organic EO material JRD1, which has a chromophore structure similar to that of YLD124 [12]. Note that the slot width $w_s = 100$ nm in our device is smaller, which is known to reduce the poling efficiency [12].

We also measure the optical losses of our current devices. For a 1 mm long CC-SOH MZM, we obtain a fiber-to-fiber insertion loss of 19 dB, out of which an overall 10 dB are caused by the two on-chip grating couplers while 3 dB originate from other passive on-chip structures such as transport waveguides, strip-to-slot converters, and MMI couplers. The propagation loss in the CC-SOH phase shifter amounts to 6 dB/mm, which we attribute to scattering losses due to surface roughness that results from an imperfect waveguide fabrication process; see Section 2B of Supplement 1 for details. Note that these losses can be greatly reduced by optimized designs and fabrication processes [35]. Specifically, systematic optimization of strip-to-slot converters and MMI couplers may allow us to reduce the losses of these building blocks to 0.02 and 0.2 dB, respectively [30,36], leading to an overall loss contribution of less than 0.5 dB. We further expect that propagation losses in the CC-SOH phase-shifter section can be reduced to less than 0.2 dB/mm by using highly optimized waveguide fabrication procedures based on 193 nm deep-UV lithography and dry-etching processes [35]. Note that amorphous and polycrystalline BTO has relatively low absorption losses in the visible and near infrared [37–41], such that the BTO slabs directly adjacent to the Si rails should not contribute substantially to the overall propagation loss. Accounting for an additional contribution of 0.1 dB/mm from the interaction of the guided light with the gold traces of the GSG transmission line, we expect that the propagation loss in the CC-SOH phase shifter may eventually be reduced to less than 0.3 dB/mm. Assuming a 1 mm long CC-SOH phase shifter and taking into account an additional 0.5 dB of loss from the strip-to-slot converters and MMI couplers [30,36], on-chip insertion losses of the order of 1 dB might eventually come into reach, which can very well compete with low-loss RC-SOH devices of much lower bandwidth [20]. Fiber-chip and chip-chip coupling losses can be greatly reduced by using 3D-printed micro-lenses [42] or photonic wire bonds [43,44].

To measure the frequency response of the CC-SOH MZM, the wavelength is adjusted for operation in the quadrature point. An RF drive signal with frequency in the range between 0.01 GHz and 110 GHz is supplied by a vector network analyzer (VNA, Keysight PNA-XN5247) and is coupled to the GSG transmission line of the MZM using a microwave probe. The other end of the transmission line is connected to another microwave probe, which is terminated by a 50 Ω impedance. The intensity-modulated output of the CC-SOH MZM is received by a calibrated high-speed photodiode

(HHI, C05-W36) having a 3 dB bandwidth of 78 GHz, which is connected to second port of the VNA. The measured data is corrected by accounting for the frequency response of the photodiode, probes, and RF cables, leading to the electro-optic (EO) response $S_{21,EO}$ of the CC-SOH MZM; see red curve in Fig. 2(d). For a 1 mm long BTO-based CC-SOH MZM, we measure a 3 dB EO bandwidth of approximately 76 GHz. Note that the 3 dB EO bandwidth corresponds to a frequency at which the phase-modulation index is reduced by a factor of $1/\sqrt{2}$, corresponding to a 3 dB decay in the associated RF power generated by the photodiode. Alternatively, the bandwidth can be specified in terms of the 6 dB bandwidth, which corresponds to a power decay of the associated photocurrent by a factor of 4 and amounts to approximately 110 GHz for the current device. In the literature [14,45–49] of EO modulators, both conventions of bandwidth are used, often without an explicit mention of the adopted specification.

Note that the bandwidth measured for the current MZM is not limited by the device concept but is a consequence of the non-optimum electrical design of our first-generation structures. Specifically, as just described, the metal transmission line is fabricated using a lift-off process with a thin photoresist, which limits the thickness of the gold layer to a rather small value of approximately 150 nm. This leads to significant RF propagation loss, which increases strongly with frequency. To better understand the underlying bandwidth limitations, we perform a detailed evaluation [50] of the device dynamics. In the first step, we measure the electrical S -parameters of the CC-SOH modulator, in particular the frequency-dependent complex amplitude reflection factor \underline{S}_{11} at the input and the complex amplitude transmission factor \underline{S}_{21} . From the measured S -parameters, we then derive the line impedance, RF propagation loss, and RF propagation constant, which is associated with the RF effective refractive index $n_{e,RF}$. Adopting the analytical model described in [29], we predict the EO response of the CC-SOH device which would be expected based on the electrical behavior; see Section 3C of Supplement 1 for details. This analysis includes the contribution due to the losses of the underlying RF transmission line, impedance mismatch, as well as the walk-off between the RF modulation signal and optical signal. The results of this analysis, indicated as a blue trace in Fig. 2(d), agree well with the directly measured EO response of the device, red trace, and we conclude that the decay of the EO response mainly originates from the electrical behavior of the RF line. We also find that walk-off between the RF signal and the optical signal does not represent a significant limitation of the current devices: based on an optical group refractive index $n_{g,opt} = 2.8$ at 1550 nm and an RF effective index $n_{e,RF} = 2.2$, we estimate a walk-off-related 3 dB bandwidth of approximately 220 GHz [51]; see Section 3C of Supplement 1 for details. As a consequence, high-RF propagation loss remains as the most important reason for the strong decay in the frequency response of our first-generation CC-SOH devices.

The RF propagation loss has two main contributions: conductor loss and dielectric loss. To investigate the contribution from the dielectric loss of BTO, we analyze the RF properties of our BTO thin films; see Sections 2D and 2E of Supplement 1 for details. We determine a frequency-independent relative permittivity $\epsilon_{r,BTO} = 18$ and a loss tangent $\tan \delta_{BTO} \approx 0.03$, which are in good agreement with previously reported measurements of amorphous BTO films [52–55]. At a frequency of 50 GHz, this loss tangent would lead to a dielectric loss less than 0.4 dB/mm in bulk BTO, which is much smaller than the overall RF propagation

loss of 4.5 dB/mm measured for the fabricated CC-SOH MZM; see Fig. S7 in Section 3C of Supplement 1. We hence conclude that the ohmic loss of our transmission-line traces dominates the attenuation of the modulating signal, which is confirmed by an electrical simulation (CST Microwave Studio) of a transmission line built from 150 nm thick gold transmission traces with a conductivity of 2.6×10^7 S/m; see Section 3C of Supplement 1 for details. The conductor loss can be significantly reduced by using thicker gold layers for the transmission line electrodes. For such an improved design of a CC-SOH modulator having a 600 nm thick metal electrodes, the 3 dB bandwidth of the 1 mm long CC-SOH MZM can be significantly higher than 100 GHz; see green curve in Fig. 2(d). Details on the advanced device designs can be found in Section 5 of Supplement 1.

Besides increased modulation bandwidth, our first-generation CC-SOH modulators also leave room for improving the modulation efficiency. The $U_\pi L$ product of the devices may be greatly reduced by using polycrystalline BTO layers with relative permittivity $\epsilon_{r,BTO} \geq 100$ [53,55], which is much larger than the value of $\epsilon_{r,BTO} = 18$ measured for our current devices. This results in a much better confinement of the modulating RF field to the slot, which, in combination with increased heights of the BTO slabs of $h_{hk} \geq 400$ nm, will lead to a more than three-fold increase of the field interaction factor from the current value of $\Gamma_s = 0.048$ to values of $\Gamma_s = 0.17$; see Fig. S10(a) in Section 5 of Supplement 1 for details. Moreover, the Si rails might be slightly doped to further improve the confinement of the RF field mode to EO material in the slot, allowing for field interaction factors $\Gamma_s > 0.3$, which are comparable to those obtained by conventional RC-SOH devices. A more detailed analysis of these approaches to improve the field interaction factor can be found Section 5 of Supplement 1. In addition, we may use more efficient EO materials such as JRD1 [34], for which in-device EO coefficients of 390 pm/V have been demonstrated in conventional RC-SOH devices with 160 nm wide slots [12]. Combining all these improvements, we would hence expect that the current $U_\pi L$ product of approximately 1.3 Vmm could be reduced by at least factor of 3, such that values of less than 0.5 Vmm can be expected. This brings sub-1 V drive voltages for sub-1 mm device lengths into reach.

4. HIGH-SPEED SIGNALING EXPERIMENTS

Figure 3(a) shows the setup for evaluating the performance of a CC-SOH MZM in high-speed data transmission. The electrical drive signals are synthesized by a 120 GSa/s arbitrary-waveform generator (AWG, Keysight M8194A) with an analog bandwidth of 45 GHz. We use a pseudo-random bit sequence (length $2^{11} - 1$) along with pulse shapes featuring a raised-cosine power spectrum to generate two- and four-level electrical signals at symbol rates of 64 Gbd and 100 Gbd. The drive signals are fed to an RF amplifier (Centellax, UA1L65VM) followed by a 6 dB attenuator before being coupled to the GSG pads of the CC-SOH MZM via a microwave probe (Cascade Microtech, i67A, 67 GHz bandwidth) and a bias-tee. The other end of the GSG transmission line is terminated with a 50 Ω impedance via a second microwave probe. In addition to the wavelength adjustment of the operating point in the unbalanced CC-SOH MZM, a DC voltage U_{bias} is applied via the bias tee for fine-tuning. For generating high-speed optical signals, an optical carrier at a wavelength near 1550 nm with input optical powers between 8 and 10 dBm is provided by an external cavity laser (ECL) and adjusted in polarization using a fiber-based

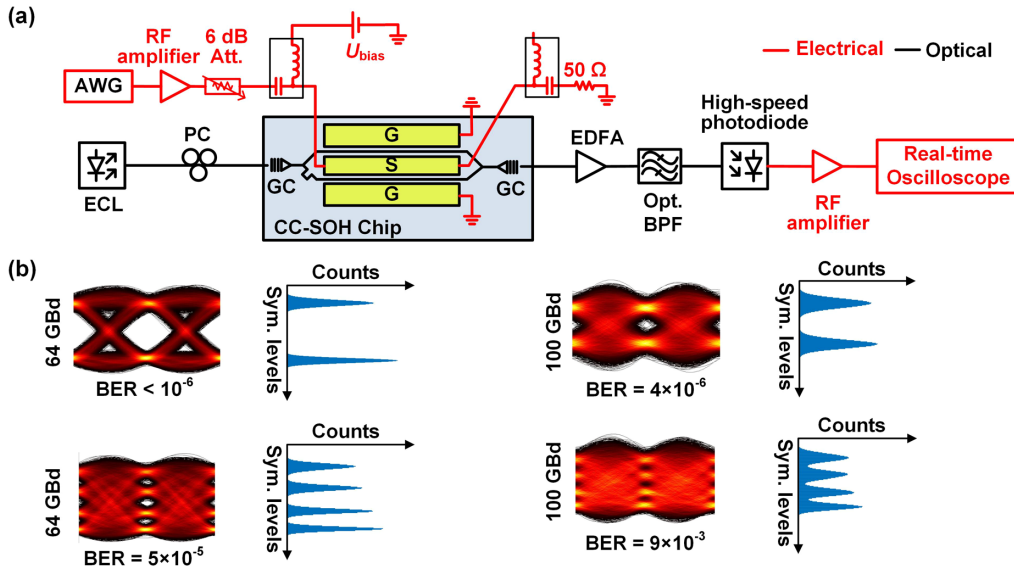


Fig. 3. High-speed signaling with a CC-SOH MZM using BTO as a high-k dielectric. (a) Setup for data signal generation and detection. An arbitrary-waveform generator (AWG) followed by an RF amplifier and 6 dB attenuator are used to drive the modulator. The electrical drive signal is fed to the ground–signal–ground (GSG) coplanar transmission line via a microwave probe (not shown). The operating point of the MZM with unbalanced arm lengths is set by the optical wavelength and fine-tuned by a DC voltage U_{bias} applied through a bias tee. Light from an external-cavity laser (ECL) is coupled to the CC-SOH MZM via a polarization controller (PC) and an on-chip grating coupler (GC). An erbium-doped fiber amplifier (EDFA) is used to amplify the light from the output GC, and a band-pass filter (Opt. BPF) suppresses the amplified spontaneous emission (ASE) noise, before a high-speed photodiode receives the light. The RF signal from the photodiode is amplified and captured by a real-time oscilloscope (RTO). (b) Eye diagrams for symbol rates of 64 GBd and 100 GBd along with the histograms of the amplitudes in the sampling point and with measured bit error ratios (BERs). At 64 GBd, the BER is below 10^{-6} for on-off keying (OOK) and reaches 5×10^{-5} for four-state pulse amplitude modulation (PAM4). At 100 GBd OOK, a BER of 4×10^{-6} is measured, well below the forward error correction (FEC) limit for 7% overhead. For 100 GBd PAM4 (line rate 200 Gbit/s), we measure a BER of 9×10^{-3} , which is still below the threshold for soft-decision FEC (SD-FEC) limit with 20% overhead.

polarization controller (PC). Light is coupled in and out of the CC-SOH MZM via on-chip grating couplers (GC). The intensity-modulated output of the MZM is amplified by an erbium-doped fiber amplifier (EDFA), and the out-of-band amplified spontaneous emission (ASE) noise is suppressed by an optical band-pass filter (Opt. BPF) with a 2 nm passband. The signal is finally fed to a high-speed photodiode having a bandwidth of 70 GHz (Finisar XPDV3120R). The resulting electrical signal is first boosted using an RF amplifier and then recorded by a 100 GHz real-time oscilloscope. For generating the electrical drive signals, we use digital pre-emphasis to compensate for the frequency roll-off of the AWG, the subsequent RF amplifier, the 6 dB attenuator, and the bias-tee; see Section 4 of Supplement 1 for details. Note that the pre-emphasis does not correct for the frequency roll-off of the CC-SOH MZM itself. The modulator is biased at the quadrature point such that the modulation loss amounts to approximately 3 dB. The modulated optical signal is amplified to an average power of about 8 dBm at the input of the receiver photodiode. In the transmission experiments, the modulator is driven by a signal with a maximum peak-to-peak voltage swing of approximately $1 V_{pp}$, calculated from the RF power at the output of the bias-tee and from the losses of approximately 1.2 dB of the RF probe at 50 GHz.

Figure 3(b) shows the eye diagrams and histograms of the detected amplitudes at the sampling point for symbol rates of 64 and 100 GBd. For 64 GBd on-off keying (OOK), no bit errors could be measured in our 15 μ s long recordings, which contain approximately 10^6 symbols. We hence estimate a bit error ratio (BER) below 10^{-6} . At 100 GBd OOK (100 Gbit/s line rate), a BER of 4×10^{-6} is measured, which is well below the hard-decision forward error correction [56] (HD-FEC) limit with 7%

overhead. For 64 GBd four-state pulse amplitude modulation (PAM4), we measure a BER of 5×10^{-5} , which is also below the FEC hard-decision FEC threshold with 7% overhead. For 100 GBd PAM4 signaling with a line rate of 200 Gbit/s, we obtain a BER of 9×10^{-3} , which is below the threshold for soft-decision FEC (SD-FEC) limit with 20% overhead. We find that the rather high BER for 100 GBd PAM4 signaling is mainly caused by the low quality of the electrical drive signal, for which a BER of 1.7×10^{-3} was measured in an electrical back-to-back experiment, in which the output of the RF amplifier was attenuated and then fed directly to the real-time oscilloscope. Still, the demonstrated performance of our first-generation CC-SOH MZM is already on par with that of advanced RC-SOH devices [20], in which the RC time constant is reduced by applying a gate voltage of approximately 200 V across the 2 μ m thick buried-oxide layer to induce a highly conductive electron accumulation layer that increases the slab conductivity [13].

5. SUMMARY

We demonstrated a novel concept for SOH electro-optic modulators that relies on a capacitive coupling scheme to overcome the intrinsic bandwidth limitation of conventional devices with resistively coupled slot waveguides. In a proof-of-concept experiment using amorphous $BaTiO_3$ as a high-k dielectric for enhanced capacitive coupling, we demonstrated a CC-SOH MZM having a 3 dB EO bandwidth of 76 GHz. The device features a small π -voltage-length product $U_\pi L = 1.3$ V mm. The viability of the CC-SOH modulator is demonstrated in a high-speed data transmission experiment, in which we generate PAM4 signals at

line rates up to 200 Gbit/s. These results are obtained with first-generation devices that leave vast room for further improvements with respect to modulation efficiency, bandwidth, and optical loss. We therefore believe that the CC-SOH concept offers an attractive route towards highly efficient silicon photonic modulators that combine sub-1 mm device lengths with sub-1 V drive voltages, sub-1 dB insertion losses, and modulation bandwidths of 100 GHz or more.

Funding. European Research Council (TeraSHAPE 773248); Deutsche Forschungsgemeinschaft (PACE 403188360, GOSPEL 403187440, HIPES 383043731) within the Priority Programme “Electronic-Photonic Integrated Systems for Ultrafast Signal Processing” (SPP 2111); European Union’s Horizon 2020 Framework Programme (TeraSlice 863322); Alfried Krupp von Bohlen und Halbach-Stiftung; Karlsruhe School of Optics Photonics; Karlsruhe Nano Micro Facility; European Regional Development Fund; National Science Foundation (DMR-1303080); Air Force Office of Scientific Research (FA9550-19-1-0069).

Acknowledgment. The authors would like to extend thanks to Alexander Kotz for help with the DC measurements of amorphous BTO films, Jochen Schäfer for help with the VNA calibration, and Keysight Technologies for an equipment loan. We thank the anonymous reviewers for their careful reviews and detailed comments. This work is supported by the European Research Council (ERC) consolidator grant for TeraSHAPE (#773248); by the Deutsche Forschungsgemeinschaft (DFG) projects PACE (#403188360) and GOSPEL (#403187440) within the Priority Programme “Electronic-Photonic Integrated Systems for Ultrafast Signal Processing” (SPP 2111), by the DFG project HIPES (#383043731); by the project TeraSlice (#863322) under European Union’s Horizon 2020 research and innovation programme, by the Alfried Krupp von Bohlen und Halbach-Stiftung; by the Karlsruhe School of Optics & Photonics (KSOP); by the Karlsruhe Nano Micro Facility (KNMF); by the European Regional Development Fund (ERDF), by the National Science Foundation (NSF) (DMR-1303080); and by the Air Force Office of Scientific Research (AFOSR) (FA9550-19-1-0069).

Disclosures. The authors declare no conflicts of interest.

Supplemental document. See Supplement 1 for supporting content.

REFERENCES

- C. Weimann, P. C. Schindler, R. Palmer, S. Wolf, D. Bekele, D. Korn, J. Pfeifle, S. Koeber, R. Schmogrow, L. Alloatti, D. Elder, H. Yu, W. Bogaerts, L. R. Dalton, W. Freude, J. Leuthold, and C. Koos, “Silicon-organic hybrid (SOH) frequency comb sources for terabit/s data transmission,” *Opt. Express* **22**, 3629–3637 (2014).
- S. Lange, S. Wolf, J. Lutz, L. Altenhain, R. Schmid, R. Kaiser, M. Schell, C. Koos, and S. Randel, “100 Gb/s intensity modulation and direct detection with an InP-based monolithic DFB laser Mach-Zehnder modulator,” *J. Lightwave Technol.* **36**, 97–102 (2018).
- A. Melikyan, N. Kaneda, K. Kim, N. B. Labs, and H. Road, “100 Gbaud QAM signaling with silicon photonic electro-absorption modulators,” in *45th European Conference on Optical Communication* (2019), paper PD2.5.
- C. Weimann, M. Laueremann, F. Hoeller, W. Freude, and C. Koos, “Silicon photonic integrated circuit for fast and precise dual-comb distance metrology,” *Opt. Express* **25**, 30091–30104 (2017).
- D. Marpaung, J. Yao, and J. Capmany, “Integrated microwave photonics,” *Nat. Photonics* **13**, 80–90 (2019).
- S. Ummethala, T. Harter, K. Koehnle, Z. Li, S. Muehlbrandt, Y. Kutuvantavida, J. Kemal, P. Marin-Palomo, J. Schaefer, A. Tessmann, S. K. Garlapati, A. Bacher, L. Hahn, M. Walther, T. Zwick, S. Randel, W. Freude, and C. Koos, “THz-to-optical conversion in wireless communications using an ultra-broadband plasmonic modulator,” *Nat. Photonics* **13**, 519–524 (2019).
- K. Giewont, K. Nummy, F. A. Anderson, J. Ayala, T. Barwicz, Y. Bian, K. K. Dezfulian, D. M. Gill, T. Houghton, S. Hu, B. Peng, M. Rakowski, S. R. Ili, J. C. Rosenberg, A. Sahin, I. Stobert, and A. Stricker, “300-mm monolithic silicon photonics foundry technology,” *IEEE J. Sel. Top. Quantum Electron.* **25**, 2908790 (2019).
- J. Witzens, “High-speed silicon photonics modulators,” *Proc. IEEE* **106**, 2158–2182 (2018).
- S. S. Azadeh, F. Merget, S. Romero-García, A. Moscoso-Mártir, N. von den Driesch, J. Müller, S. Mantl, D. Buca, and J. Witzens, “Low V_{π} silicon photonics modulators with highly linear epitaxially grown phase shifters,” *Opt. Express* **23**, 23526–23550 (2015).
- C. Koos, J. Brosi, M. Waldow, W. Freude, and J. Leuthold, “Silicon-on-insulator modulators for next-generation 100 Gbit/s-Ethernet,” in *33rd European Conference and Exhibition of Optical Communication* (2007), pp. 1–2.
- C. Koos, J. Leuthold, W. Freude, M. Kohl, L. Dalton, S. Member, W. Bogaerts, A. L. Giesecke, M. Laueremann, A. Melikyan, S. Koeber, S. Wolf, C. Weimann, S. Muehlbrandt, K. Koehnle, J. Pfeifle, W. Hartmann, Y. Kutuvantavida, S. Ummethala, R. Palmer, D. Korn, L. Alloatti, P. C. Schindler, D. L. Elder, T. Wahlbrink, and J. Bolten, “Silicon-organic hybrid (SOH) and plasmonic-organic hybrid (POH) integration,” *J. Lightwave Technol.* **34**, 256–268 (2016).
- C. Kieninger, Y. Kutuvantavida, D. L. Elder, S. Wolf, H. Zwickel, M. Blaicher, J. N. Kemal, M. Laueremann, S. Randel, W. Freude, L. R. Dalton, and C. Koos, “Ultra-high electro-optic activity demonstrated in a silicon-organic hybrid (SOH) modulator,” *Optica* **5**, 739–748 (2018).
- L. Alloatti, R. Palmer, S. Diebold, K. P. Pahl, B. Chen, R. Dinu, M. Fournier, J. M. Fedeli, T. Zwick, W. Freude, C. Koos, and J. Leuthold, “100 GHz silicon-organic hybrid modulator,” *Light Sci. Appl.* **3**, e173 (2014).
- H. Zwickel, S. Singer, C. Kieninger, Y. Kutuvantavida, N. Muradyan, T. Wahlbrink, S. Yokoyama, S. Randel, W. Freude, and C. Koos, “Verified equivalent-circuit model for slot-waveguide modulators,” *Opt. Express* **28**, 12951–12976 (2020).
- S. Wolf, H. Zwickel, W. Hartmann, M. Laueremann, Y. Kutuvantavida, C. Kieninger, L. Altenhain, R. Schmid, J. Luo, A. K. Y. Jen, S. Randel, W. Freude, and C. Koos, “Silicon-organic hybrid (SOH) Mach-Zehnder modulators for 100 Gbit/s on-off keying,” *Sci. Rep.* **8**, 2598 (2018).
- A. Melikyan, L. Alloatti, A. Muslija, D. Hillerkuss, P. C. Schindler, J. Li, R. Palmer, D. Korn, S. Muehlbrandt, D. Van Thourhout, B. Chen, R. Dinu, M. Sommer, C. Koos, M. Kohl, W. Freude, and J. Leuthold, “High-speed plasmonic phase modulators,” *Nat. Photonics* **8**, 229–233 (2014).
- C. Haffner, W. Heni, Y. Fedoryshyn, J. Niegemann, A. Melikyan, D. L. Elder, B. Baeuerle, Y. Salamin, A. Josten, U. Koch, C. Hoessbacher, F. Ducry, L. Juchli, A. Emboras, D. Hillerkuss, M. Kohl, L. R. Dalton, C. Hafner, and J. Leuthold, “All-plasmonic Mach-Zehnder modulator enabling optical high-speed communication at the microscale,” *Nat. Photonics* **9**, 525–528 (2015).
- M. Burla, C. Hoessbacher, W. Heni, C. Haffner, Y. Fedoryshyn, D. Werner, T. Watanabe, H. Massler, D. L. Elder, L. R. Dalton, and J. Leuthold, “500 GHz plasmonic Mach-Zehnder modulator enabling sub-THz microwave photonics,” *APL Photon.* **4**, 056106 (2019).
- C. Haffner, W. Heni, D. L. Elder, Y. Fedoryshyn, N. Đorđević, D. Chelladurai, U. Koch, K. Portner, M. Burla, B. Robinson, L. R. Dalton, and J. Leuthold, “Harnessing nonlinearities near material absorption resonances for reducing losses in plasmonic modulators,” *Opt. Mater. Express* **7**, 2168–2181 (2017).
- C. Kieninger, C. Füllner, H. Zwickel, Y. Kutuvantavida, J. N. Kemal, C. Eschenbaum, D. L. Elder, L. R. Dalton, W. Freude, S. Randel, and C. Koos, “Silicon-organic hybrid (SOH) Mach-Zehnder modulators for 100 Gb/s PAM4 signaling with sub-1 dB phase-shifter loss,” *Opt. Express* **28**, 24693–24707 (2020).
- C. Wang, M. Zhang, X. Chen, M. Bertrand, A. Shams-Ansari, S. Chandrasekhar, P. Winzer, and M. Lončar, “Integrated lithium niobate electro-optic modulators operating at CMOS-compatible voltages,” *Nature* **562**, 101–106 (2018).
- Y. Ogiso, J. Ozaki, Y. Ueda, H. Wakita, M. Nagatani, H. Yamazaki, M. Nakamura, T. Kobayashi, S. Kanazawa, and Y. Hashizume, “80-GHz bandwidth and 1.5-V V_{π} InP-based IQ modulator,” *J. Lightwave Technol.* **38**, 249–255 (2020).
- S. Ummethala, J. N. Kemal, M. Laueremann, A. S. Alam, H. Zwickel, T. Harter, Y. Kutuvantavida, L. Hahn, S. H. Nandam, D. L. Elder, L. R. Dalton, W. Freude, S. Randel, and C. Koos, “Capacitively coupled silicon-organic hybrid modulator for 200 Gbit/s PAM-4 signaling,” in *Conference on Lasers and Electro-Optics* (2019), paper JTh5B.2.
- V. R. Almeida, Q. Xu, C. A. Barrios, and M. Lipson, “Guiding and confining light in void nanostructure,” *Opt. Lett.* **29**, 1209–1211 (2004).
- S. Wolf, M. Laueremann, P. Schindler, G. Ronniger, K. Geister, R. Palmer, and K. Sebastian, “DAC-less amplifier-less generation and transmission of QAM signals using sub-volt silicon-organic hybrid modulators,” *J. Lightwave Technol.* **33**, 1425–1432 (2015).

26. S. Wolf, H. Zwickel, C. Kieninger, M. Lauermann, W. Hartmann, Y. Kutuvantavida, W. Freude, S. Randel, and C. Koos, "Coherent modulation up to 100 Gb/s using silicon-organic hybrid (SOH) devices," *Opt. Express* **26**, 220–232 (2018).
27. H. Zwickel, S. Wolf, C. Kieninger, Y. Kutuvantavida, M. Lauermann, T. de Keulenaer, A. Vyncke, R. Vaerenwyck, J. Luo, A. K.-Y. Jen, W. Freude, J. Bauwelinck, S. Randel, and C. Koos, "Silicon-organic hybrid (SOH) modulators for intensity-modulation/direct-detection links with line rates of up to 120 Gbit/s," *Opt. Express* **25**, 23784–23800 (2017).
28. S. Shi and D. W. Prather, "Ultrabroadband electro-optic modulator based on hybrid silicon-polymer dual vertical slot waveguide," *Adv. Optoelectron.* **2011**, 714895 (2011).
29. S. H. Lin and S.-Y. Wang, "High-throughput GaAs PIN electrooptic modulator with a 3-dB bandwidth of 96 GHz at 1.3 μm ," *Appl. Opt.* **26**, 1696–1700 (1987).
30. R. Palmer, L. Alloatti, D. Korn, W. Heni, P. C. Schindler, J. Bolten, M. Karl, M. Waldow, T. Wahlbrink, W. Freude, C. Koos, and J. Leuthold, "Low-loss silicon strip-to-slot mode converters," *IEEE Photon. J.* **5**, 2200409 (2013).
31. J. Golden, H. Miller, D. Nawrocki, and J. Ross, "Optimization of Bi-layer lift-off resist process," in *International Conference on Compound Semiconductor Manufacturing Technology (CS MANTECH)* (2009).
32. S. Krátký, M. Horáček, P. Meluzín, V. Kolařík, M. Matějka, J. Oulehla, and Z. Pešić, "Lift-off technology for thick metallic microstructures," in *26th International Conference on Metallurgy and Materials (METAL)* (2017), pp. 1298–1302.
33. W. Heni, C. Haffner, D. L. Elder, A. F. Tillack, Y. Fedoryshyn, R. Cottier, Y. Salamin, C. Hoessbacher, U. Koch, B. Cheng, B. Robinson, L. R. Dalton, and J. Leuthold, "Nonlinearities of organic electro-optic materials in nanoscale slots and implications for the optimum modulator design," *Opt. Express* **25**, 2627–2653 (2017).
34. W. Jin, P. V. Johnston, D. L. Elder, A. F. Tillack, B. C. Olbricht, J. Song, P. J. Reid, R. Xu, B. H. Robinson, and L. R. Dalton, "Benzocyclobutene barrier layer for suppressing conductance in nonlinear optical devices during electric field poling," *Appl. Phys. Lett.* **104**, 243304 (2014).
35. S. K. Selvaraja, P. De Heyn, G. Winroth, P. Ong, G. Lepage, C. Cailler, A. Rigny, K. K. Bourdelle, W. Bogaerts, D. Van Thourhout, J. Van Campenhout, and P. Absil, "Highly uniform and low-loss passive silicon photonics devices using a 300 mm CMOS platform," in *Optical Fiber Communication Conference (OFC)* (2014), paper Th2A.33.
36. W. Bogaerts, S. K. Selvaraja, P. Dumon, J. Brouckaert, K. De Vos, D. Van Thourhout, and R. Baets, "Silicon-on-insulator spectral filters fabricated with CMOS technology," *IEEE J. Sel. Top. Quantum Electron.* **16**, 33–44 (2010).
37. L. Scholtz, P. Šutta, P. Calta, P. Novák, M. Solanská, and J. Müllerová, "Investigation of barium titanate thin films as simple antireflection coatings for solar cells," *Appl. Surf. Sci.* **461**, 249–254 (2018).
38. M. Cardona, "Optical properties and band structure of SrTiO₃ and BaTiO₃," *Phys. Rev.* **140**, A651–A655 (1965).
39. J. Xu, J. Zhai, X. Yao, J. Xue, and Z. Huang, "Dielectric and optical properties of BaTiO₃ thin films prepared by low-temperature process," *J. Sol-Gel Sci. Technol.* **42**, 209–212 (2007).
40. A. Karvounis, F. Timpu, V. V. Vogler-Neuling, R. Savo, and R. Grange, "Barium titanate nanostructures and thin films for photonics," *Adv. Opt. Mater.* **8**, 1–23 (2020).
41. A. K. Sharma, B. G. Priyadarshini, B. R. Mehta, and D. Kumar, "An amorphous barium titanate thin film improves light trapping in Si solar cells," *RSC Adv.* **5**, 59881–59886 (2015).
42. P. I. Dietrich, M. Blaicher, I. Reuter, M. Billah, T. Hoose, A. Hofmann, C. Caer, R. Dangel, B. Offrein, U. Troppenz, M. Moehrl, W. Freude, and C. Koos, "In situ 3D nanoprinting of free-form coupling elements for hybrid photonic integration," *Nat. Photonics* **12**, 241–247 (2018).
43. M. Billah, M. Blaicher, T. Hoose, P. I. Dietrich, P. Marin-Palomo, N. Lindenmann, A. Nestic, A. Hofmann, U. Troppenz, M. Moehrl, S. Randel, W. Freude, and C. Koos, "Hybrid integration of silicon photonic circuits and InP lasers by photonic wire bonding," *Optica* **5**, 876–883 (2018).
44. M. Blaicher, M. R. Billah, J. Kemal, T. Hoose, P. Marin-Palomo, A. Hofmann, Y. Kutuvantavida, C. Kieninger, P. I. Dietrich, M. Lauermann, S. Wolf, U. Troppenz, M. Moehrl, F. Merget, S. Skacel, J. Witzens, S. Randel, W. Freude, and C. Koos, "Hybrid multi-chip assembly of optical communication engines by in situ 3D nano-lithography," *Light Sci. Appl.* **9**, 71 (2020).
45. H. Chung, W. S. C. Chang, and E. L. Adler, "Modeling and optimization of traveling-wave LiNbO₃ interferometric modulators," *IEEE J. Quantum Electron.* **27**, 608–617 (1991).
46. H. Yu and W. Bogaerts, "An equivalent circuit model of the traveling wave electrode for carrier-depletion-based silicon optical modulators," *J. Lightwave Technol.* **30**, 1602–1609 (2012).
47. F. Merget, S. S. Azadeh, J. Mueller, B. Shen, M. P. Nezhad, J. Hauck, and J. Witzens, "Silicon photonics plasma-modulators with advanced transmission line design," *Opt. Express* **21**, 19593–19607 (2013).
48. K. Kawano, T. Kitoh, H. Jumonji, T. Nozawa, and M. Yanagibashi, "New travelling-wave electrode Mach-Zehnder optical modulator with 20 GHz bandwidth and 4.7 V driving voltage at 1.52 μm wavelength," *Electron. Lett.* **25**, 1382–1383 (1989).
49. I. P. Kaminow, *An Introduction to Electrooptic Devices* (Academic, 1974).
50. S. Y. Wang and S. H. Lin, "High speed III-V electro-optic waveguide modulators at $\lambda = 1.3 \mu\text{m}$," *J. Lightwave Technol.* **6**, 758–771 (1988).
51. R. G. Walker, "High-speed III-V semiconductor intensity modulators," *IEEE J. Quantum Electron.* **27**, 654–667 (1991).
52. S. S. Park, "Properties of BaTiO₃ films sputter deposited on PET for pulse power capacitors," *Ferroelectrics* **457**, 97–104 (2013).
53. Z. Q. Shi, Q. X. Jia, and W. A. Anderson, "Electrical and dielectric properties of thin film BaTiO₃ capacitors deposited by radio frequency magnetron sputtering," *J. Vac. Sci. Technol. A* **10**, 733–736 (1992).
54. W. T. Liu, S. Cochrane, X. M. Wu, P. K. Singh, X. Zhang, D. B. Knorr, J. F. McDonald, E. J. Rymaszewski, J. M. Borrego, and T. M. Lu, "Frequency domain (1 kHz–40 GHz) characterisation of thin films for multichip module packaging technology," *Electron. Lett.* **30**, 117–118 (1994).
55. Q. X. Jia, Z. Q. Shi, and W. A. Anderson, "BaTiO₃ thin film capacitors deposited by r.f. magnetron sputtering," *Thin Solid Films* **209**, 230–239 (1991).
56. F. Chang, K. Onohara, and T. Mizuochi, "Forward error correction for 100 G transport networks," *IEEE Commun. Mag.* **48**(3), S48–S55 (2010).